Available online at www.sciencedirect.com
ScienceDirect
Trans. Nonferrous Met. Soc. China 34(2024) 2313−2327
Transactions of Nonferrous Metals Society of China
www.tnmsc.cn

Peridynamic simulation of rock failure with surface flaw under dynamic loading

Jun ZHANG, Lin-qi HUANG, Zhi-xiang LIU, Xi-bing LI

School of Resources and Safety Engineering, Central South University, Changsha 410083, China

Received 22 December 2022; accepted 11 May 2023

Abstract: To investigate the propagation of surface flaws in rocks under dynamic loading, an elastic−plastic ordinary state-based peridynamic model that considers the compressive to tensile strength ratio is used for numerical tests based on the results of previous experiments. The failure process of rocks containing three-dimensional surface flaws at different angles and depths under dynamic loading is simulated. The simulation results show that the peridynamic model used can well simulate the propagation of three-dimensional cracks in rocks and the failure process of specimens. Peridynamic simulations can be used to obtain strength variation regularity which is consistent with the experimental results. The crack generated on the surface of the specimen penetrates to a certain depth inside the specimen, which is related to the depth of the surface flaw. Shell-like cracks generated inside the specimen join with cracks generated on the surface to form complex three-dimensional cracks.

Key words: dynamic loading; surface flaw; peridynamics; three-dimensional crack propagation; rock failure

1 Introduction

There are different flaws on the surface and within the rock, and most of these flaws are in three-dimensional form. The presence of these three-dimensional flaws can have an impact on the failure of the rock, and it is therefore necessary to investigate the propagation pattern of three-dimensional cracks in rocks.

In previous studies, many scholars have conducted experimental [1−3], numerical [4−6], and theoretical [7,8] studies on the propagation of two-dimensional cracks in rocks. Under plane stress or plane strain conditions, the propagation of a two-dimensional crack can be considered a simplification of a three-dimensional crack. ZHOU et al [9,10] experimentally studied three-dimensional cracks under dynamic loading. PAKZAD et al [11] used ABAQUS to simulate crack propagation in a three-dimensional cylindrical sample containing prefabricated flaws under uniaxial compression and analyzed the effect of the compressive to tensile strength ratio on the failure of the specimen. MONDAL et al [12] investigated crack propagation and failure in sandstone specimens containing surface flaws under uniaxial compression using a finite element method by taking damage evolution into account. LIANG et al [13] and QIAN et al [14,15] used rock failure process analysis (RFPA) to study the failure process of rock specimens containing different angles and multiple surface flaws under static and dynamic loading. WANG et al [16] investigated the effect of cross fissures of different shapes on the mechanical properties and failure characteristics of rocks using experiments and PFC3D. RABCZUK et al [17] proposed a mesh-free method to simulate initiation, propagation, and connection of three-dimensional cracks. LIAO et al [18] used a three-dimensional

Corresponding author: Lin-qi HUANG, Tel: +86-13469059806, E-mail: huanglinqi@csu.edu.cn
DOI: 10.1016/S1003-6326(24)66543-X

FEM-based numerical model to investigate rock plate cracking and failure under impact loading.

Peridynamics is a simulation method proposed by SILLING and ASKARI [19,20] that considers non-local effects. YU et al [21,22] proposed bond-based peridynamic models that take into account tensile−rotation−shear coupling effects and strain-rate effects and applied them to brittle materials. AI et al [23,24] used bond-based peridynamics to study the stress−strain curves and crack propagation patterns in rock Brazilian discs under dynamic loading. CHEN et al [25] proposed a bond-based peridynamics model considering initial damage for application to porous materials. DIANA et al [26] used bond-based micro-elastic peridynamics to simulate the crack initiation and propagation of rock in three-point bending tests under static conditions. ZHOU et al [27] proposed a micro-elastic−plastic bond-based peridynamic model considering post-peak damage to simulate crack propagation and failure of rocks under different compression conditions. FENG and ZHOU [28] modeled the mechanical properties and failure characteristics of granite under uniaxial compression using bond-based peridynamics, considering shear deformation. WANG et al [29] used a peridynamic model based on conjugate bonds to study three-dimensional crack propagation in rock specimens containing intermittent fractures under compression−shear conditions. ZHANG et al [30] studied the dynamic mechanical response of granular materials using the PMB model. SILLING et al [31] developed bond-based peridynamics into state-based peridynamics. YANG et al [32] used ordinary state-based peridynamics to study the crack propagation and failure characteristics of rocks containing a single non-straight fissure at different angles under static loading. BUTT and MESCHKE [33] used state-based peridynamics to study three-dimensional crack propagation in PMMA specimens containing flaws under dynamic tensile conditions. ZHOU et al [34] studied the plastic response of rock using ordinary state-based peridynamics incorporating Drucker−Prager plasticity. ZHOU et al [35,36] studied the crack initiation, propagation, and coalescence of rock using non-ordinary state-based peridynamics based on a stress damage criterion. CHEN et al [37] used state-based peridynamics to study the propagation of drill-induced borehole damage.

Rocks are commonly subjected to different dynamic loads, and the existing literature contains relatively few studies of three-dimensional crack propagation in rocks under dynamic loading. In this work, based on the results of previous experiments on dynamically loaded rocks with surface flaws [38], failure process of dynamically loaded rocks with three-dimensional surface flaws at different angles and depths is simulated using elastic−plastic ordinary state-based peridynamics, by taking into account the compressive and tensile strength ratio. By slicing the simulation results and investigating the crack propagation process inside the specimen, the three-dimensional crack propagation pattern under dynamic loading is studied.

2 Theories

2.1 Basic theory of ordinary state-based peridynamics

Peridynamics discretizes solids into material points, which interact with each other through bonds. In state-based peridynamics, the bond forces are allowed to vary in magnitude and direction. Bond forces in the same direction and different magnitudes are called ordinary state-based peridynamics. The equations of motion in state-based peridynamics are expressed as follows [31]:

$$\rho(\boldsymbol{x})\ddot{\boldsymbol{u}}(\boldsymbol{x},t)=\int_{H_x}\{\underline{\boldsymbol{T}}[\boldsymbol{x},t]\langle\boldsymbol{x}'-\boldsymbol{x}\rangle-\underline{\boldsymbol{T}}[\boldsymbol{x}',t]\langle\boldsymbol{x}-\boldsymbol{x}'\rangle\}\mathrm{d}V_{\boldsymbol{x}'}+\boldsymbol{b}(\boldsymbol{x},t) \tag{1}$$

where ρ is the mass density of the material point and $\ddot{\boldsymbol{u}}(\boldsymbol{x},t)$ is the acceleration related to material point position $\boldsymbol{x}$ and time t. $\underline{\boldsymbol{T}}$ is the force state, and the state can be interpreted as a function of vectors. $\boldsymbol{b}$ represents the body force density, and H_x is the domain of influence of the material point denoted by δ:

$$H_{\boldsymbol{x}}=H(\boldsymbol{x},\delta)=\{\underline{x'}-\underline{x}\le\delta \mid \underline{x'}\in\mathbf{R}\} \tag{2}$$

The position vector $\boldsymbol{\xi}$ and the displacement vector $\boldsymbol{\eta}$ of the material point $\boldsymbol{x}$ as it moves to $\boldsymbol{x}'$ are expressed as

$$\boldsymbol{\xi}=\boldsymbol{x}'-\boldsymbol{x} \tag{3}$$

$$\boldsymbol{\eta}=\boldsymbol{u}'(\boldsymbol{x}',t)-\boldsymbol{u}(\boldsymbol{x},t) \tag{4}$$

Then, the stretch (s) of the bond can be expressed as

$$s(\boldsymbol{\eta},\xi,t)=\frac{\|\boldsymbol{\eta}+\xi\|-\|\xi\|}{\|\xi\|} \tag{5}$$

The mechanical form of ordinary state-based peridynamics is expressed as

$$\underline{\boldsymbol{T}}=\underline{t}\,\underline{\boldsymbol{M}} \tag{6}$$

where $\underline{t}$ is the scalar force state, and $\underline{\boldsymbol{M}}$ is the vector state of the deformed direction. Ordinary state-based peridynamics has been proven to satisfy angular and linear momentum balance.

2.2 Elastic−plastic model

SILLING et al [31] proposed elastic and ideal elastic−plastic models, as shown in Fig. 1, where f_y represents the yield strength and the elastic−plastic material model is used in this work. The elastic−plastic material model in the form of rates is defined as follows:

$$\dot{\underline{t}}=\dot{\underline{t}}^{\mathrm{i}}+\dot{\underline{t}}^{\mathrm{d}} \tag{7}$$

$$\dot{\underline{t}}^{\mathrm{i}}=\frac{3k\dot{\theta}}{m}\underline{\omega x},\quad \dot{\theta}=\hat{\theta}(\dot{\underline{e}}) \tag{8}$$

$$\dot{\underline{t}}^{\mathrm{d}}=\alpha\underline{\omega}\dot{\underline{e}}^{\mathrm{de}},\quad \dot{\underline{e}}^{\mathrm{de}}=\dot{\underline{e}}^{\mathrm{d}}-\dot{\underline{e}}^{\mathrm{dp}},\quad \dot{\underline{e}}^{\mathrm{dp}}=\lambda\nabla^{\mathrm{d}}\psi \tag{9}$$

$$\lambda=\begin{cases}0, & \psi\left(\underline{t}^{\mathrm{d}}\right)<\psi_0 \text{ or } \left(\underline{\omega}\dot{\underline{e}}^{\mathrm{d}}\right)\cdot\nabla^{\mathrm{d}}\psi<0\\ \lambda^{p}, & \text{otherwise}\end{cases} \tag{10}$$

$$\lambda^{\mathrm{p}}=\frac{\left(\underline{\omega}\dot{\underline{e}}^{\mathrm{d}}\right)\cdot\nabla^{\mathrm{d}}\psi}{\left(\underline{\omega}\nabla^{\mathrm{d}}\psi\right)\cdot\nabla^{\mathrm{d}}\psi} \tag{11}$$

where $\dot{\underline{t}}$ is the scalar force state field; $\dot{\underline{t}}^{\mathrm{i}}$ and $\dot{\underline{t}}^{\mathrm{d}}$ are the co-isotropic part and co-deviatoric part of $\dot{\underline{t}}$, respectively; $\dot{\underline{e}}$ is the extension scalar state; $\dot{\theta}$ represents dilatation; $\dot{\underline{e}}^{\mathrm{d}}$ is the deviatoric part of $\dot{\underline{e}}$; ψ is a function of a state; ψ_0 is a fixed scalar; $\dot{\underline{e}}^{\mathrm{de}}$ and $\dot{\underline{e}}^{\mathrm{dp}}$ are the elastic and plastic deviatoric extension rates, respectively; $\nabla^{\mathrm{d}}\psi$ is the Frechet derivative, and ω is the influence function; m is the weighted volume, and θ characterizes the volumetric strain; α and k are parameters related to shear modulus and bulk modulus, respectively.

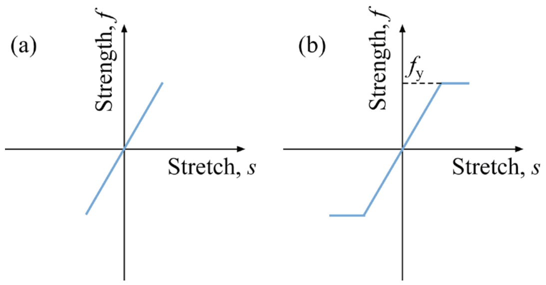

Fig. 1 Elastic (a) and elastic−plastic (b) models

2.3 Failure criteria

Figure 2(a) shows the prototype peridynamic failure criterion considering the critical tensile stretch, and the characteristic function of this criterion is expressed as

$$\mu(\boldsymbol{\eta},\xi,t)=\begin{cases}1, & s\le s_{\mathrm{c}}\\ 0, & s>s_{\mathrm{c}}\end{cases} \tag{12}$$

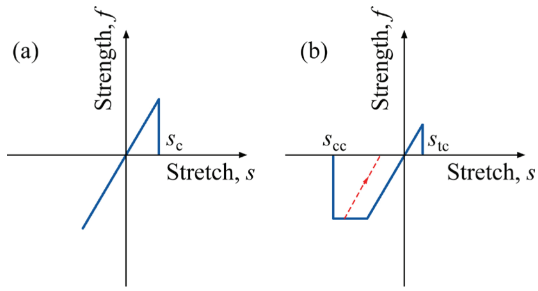

Fig. 2 Failure criteria: (a) Prototype model; (b) Elastic−plastic model (s_{c}−Critical tensile stretch; s_{cc}−Critical compression stretch; s_{tc}−Critical tensile stretch)

According to results of existing studies [39], the critical stretch in three-dimensional conditions can be written as

$$s_{\mathrm{c}}=\sqrt{\frac{G_{0\mathrm{c}}}{\left[3G+\left(\frac{3}{4}\right)^{4}\left(K-\frac{5G}{3}\right)\right]\delta}} \tag{13}$$

where $G_{0\mathrm{c}}$ is the critical energy release rate; K and G are the bulk and shear moduli in three dimensions, respectively.

Peridynamics characterizes damage in its theoretical definition through bond breakage, with the damage parameters expressed as follows:

$$D(\boldsymbol{x},t)=1-\frac{\int_{H_x}\mu(\boldsymbol{\eta},\xi,t)\mathrm{d}V}{\int_{H_x}\mathrm{d}V} \tag{14}$$

Rock is a material whose compressive strength is much greater than its tensile strength, and there is a large difference between the corresponding compressive and tensile strains at the time of failure. The failure criterion (Eq. (13)) shows that the critical stretch is related to the energy release rate, which is related to the stress and strain at failure, and should be applied to rock materials taking into account the difference between compressive and tensile strengths. In addition, rock material is also characterized by plasticity. In this work, an elastic−plastic ordinary state-based peridynamic failure criterion that takes into account the compressive and tensile strength ratio as shown in Fig. 2(b) is used, and the code for the failure criterion is rewritten. With positive stretch in tension and negative stretch in compression, the characteristic function is modified as follows:

$$\mu(\boldsymbol{\eta},\boldsymbol{\xi},t)=\begin{cases}1, s_{cc}\le s\le s_{tc}\\0, s>s_{tc} \text{ or } s<s_{cc}\end{cases} \tag{15}$$

ZOU et al [40] showed that the compressive and tensile strengths of rocks under dynamic loading increased differently with strain rate, with the dynamic tensile strength increasing more rapidly with dynamic strain rate. The tensile strength of the simulated rock in static conditions is approximately 1/10 of the compressive strength, but in dynamic conditions the tensile strength increases more rapidly, leading to an increase in this ratio. After trying out different compression and tensile strength ratios, a critical stretch of s_{cc}=4s_{tc} is used in this work.

2.4 Model setup and convergence analysis

Figure 3 shows the model used for the simulation, which is consistent with the specimen containing surface flaws used in the experiment. The model size is 30 mm× 30 mm × 30 mm, and the surface flaw depths (d) are 10, 20, and 30 mm, respectively. The surface flaw angle increases from 0° to 90° at 15° intervals. The properties of the material are set according to the experimental results using the elastic−plastic model. The dynamic yield stress is 82.0 MPa. The density of the material is 2420 kg/m^3. The bulk modulus is 5.0 GPa, and the shear modulus is 2.5 GPa. The tensile critical stretch is 0.01 and the compressive critical stretch is 0.04. The surface flaw width is 1.0 mm. The loading direction is in the y-axis direction, and the same displacement boundary conditions as in the experiment are used to achieve constant strain rate loading. An explicit solver is used with a time step of 1.3×10^{-7} s.

In order to ensure the accuracy of the numerical simulation, the model is analyzed for m-convergence and δ-convergence in conjunction with the experimental results. The experimental results of specimens containing surface flaws at an angle of 45° and a depth of d=10 mm (Fig. 11 in Ref. 38) are compared with the simulated results by varying the m (with δ fixed) and δ values (with m fixed) of the model, respectively. As the critical stretch is related to δ, the critical stretch is adjusted simultaneously when δ is changed. Figures 4 and 5 show the results of the m-convergence and δ-convergence analyses, respectively. For ease of observation, the simulation results are rotated 90° counterclockwise around the z-axis. That is to say, the up and down directions in Figs. 4(b) and 5(b) are the y-axis loading directions, and the left and right directions are the x-axis. The following sections are identical.

As can be seen from Fig. 4(a), the simulated stress−strain curves at m=3 and 4 for δ=1 mm are close to the experimental results, and the simulated maximum stress at m=2 is slightly greater than the experimental results. Figure 4(b) shows that the final failure pattern of the simulated result at m=2 is not sufficiently clear, and the failure pattern of the simulated result at m=4 differs slightly from the experimental result. When m=3, the simulated result is close to the experimental result.

As can be seen from Fig. 5(a), the simulated

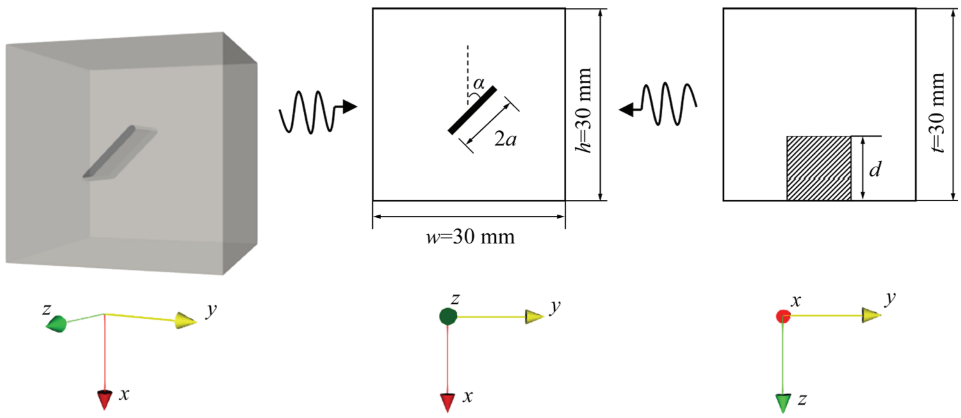

Fig. 3 Specimen models

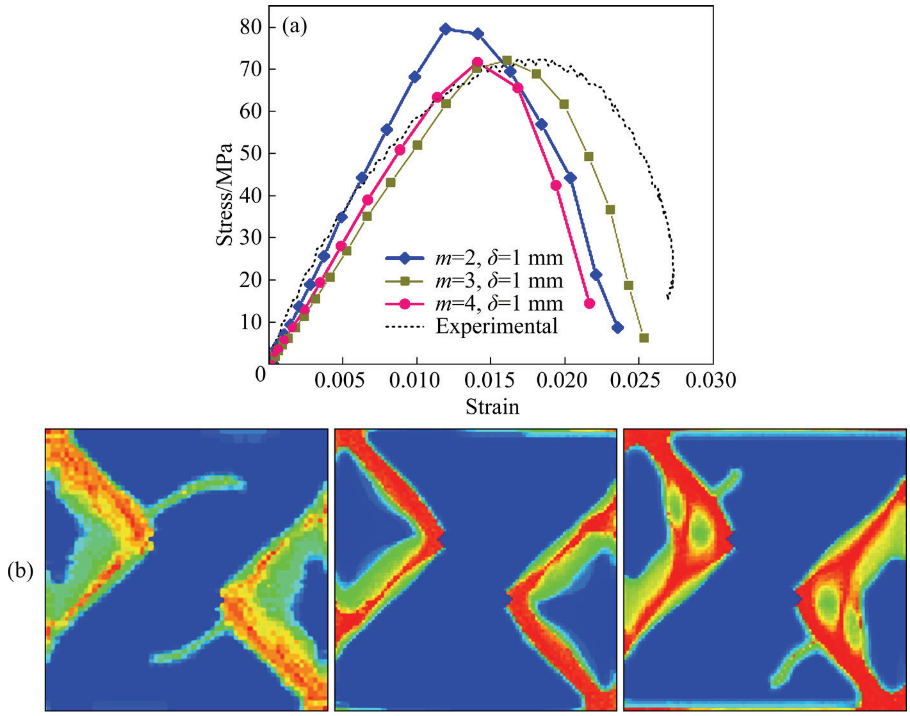

Fig. 4 *m*-convergence analysis results: (a) Simulated and experimental stress−strain curves for different *m* (δ=1 mm); (b) Failure patterns for different values of *m* (δ=1 mm)

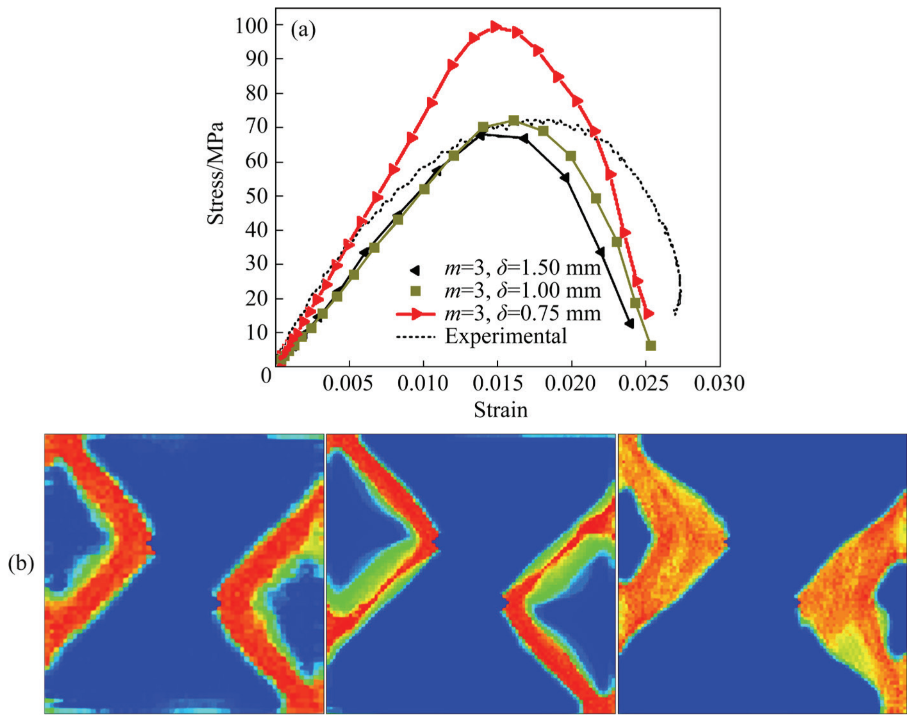

Fig. 5 δ-convergence analysis results: (a) Simulated and experimental stress−strain curves for different δ (*m*=3); (b) Failure patterns for different values of δ (*m*=3)

stress−strain curves at *m*=3, δ=1.50, and 1.00 mm are close to the experimental result, and the maximum stress at δ=0.75 mm is greater than the experimental result. Figure 5(b) shows that the simulated failure pattern is slightly coarse at δ=1.50 mm. At δ=1.00 mm, the simulated failure pattern is close to the experimental result. At δ=0.75 mm, the strength and damage zone increase, resulting in a change in the failure pattern.

The results of the convergence analysis show that the stress−strain curves and failure modes for m=3 and δ=1.00 mm are in good agreement with the experimental results. Therefore, m=3 and δ=1.00 mm are used eventually in this work for the simulation study, with a model Δx of 0.33 mm. In the computation, m is taken to be slightly greater than 3, as δ=3.015Δx [20]. Each model has approximately 720000 material points.

3 Simulation results and discussion

3.1 Mechanical properties

Figure 6 shows the simulated and experimental stress−strain curves for specimens containing surface flaws at different angles and depths. As can be seen from Fig. 6, the angle of the surface flaw has different effects on specimens containing different depths of surface flaws. As the surface flaw depth increases, the dynamic strength and strain of the specimen decrease.

Figure 7 shows the simulated and experimental dynamic strength results for specimens containing surface flaws at different angles and depths. The simulated results for dynamic strength are in good agreement with the experimental results. The simulation results for specimens containing three different depths of surface flaws all show the lowest strength at a surface flaw angle of 0° and the highest strength at an angle of 90°. The strength of the specimens all increases as the angle of the surface flaw increases. At surface flaw angles less than 60°, the dynamic strength of the specimen decreases significantly as the depth of the surface flaw increases. At surface flaw angles of 75° and 90°, the effect of the depth of the surface flaw on the strength of the specimen decreases. The results

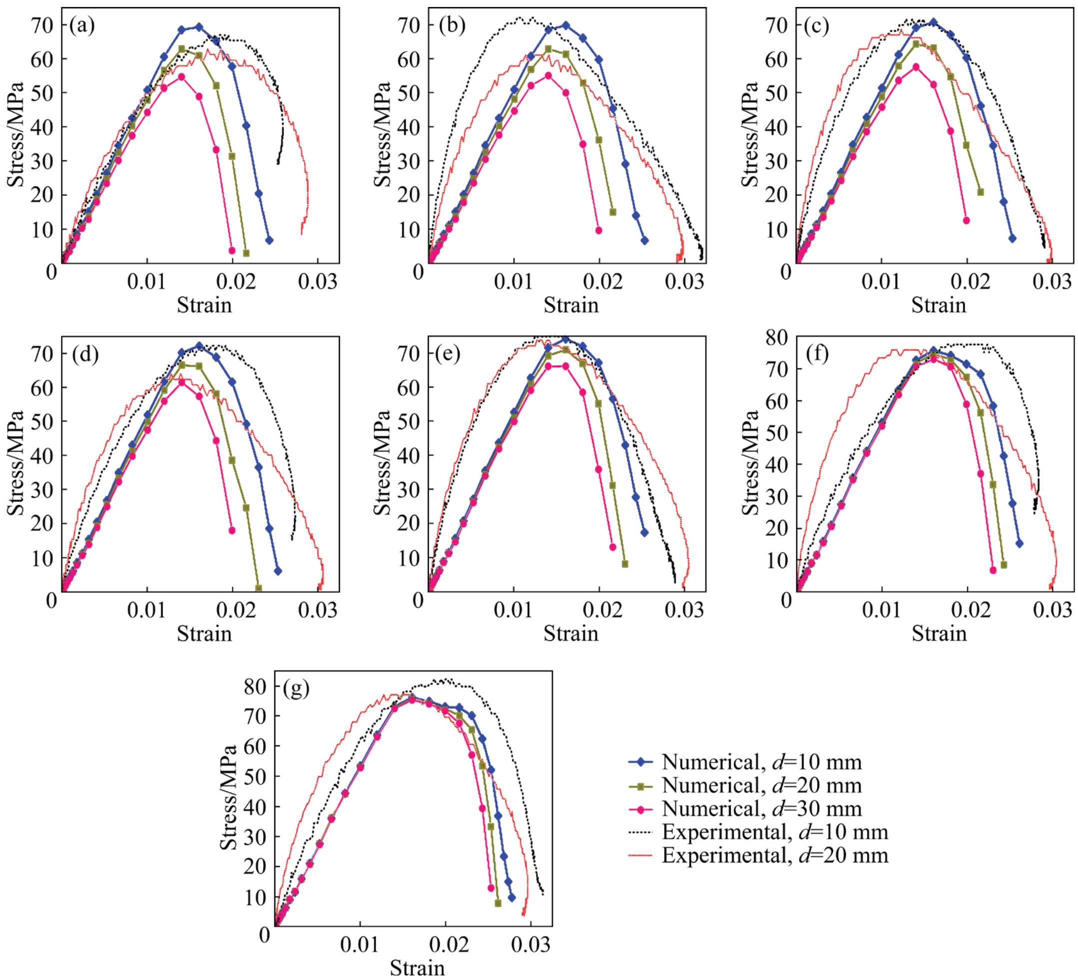

Fig. 6 Results of numerical and experimental stress−strain curves for specimens containing surface flaws at different angles and depths: (a) α=0°; (b) α=15°; (c) α=30°; (d) α=45°; (e) α=60°; (f) α=75°; (g) α=90°

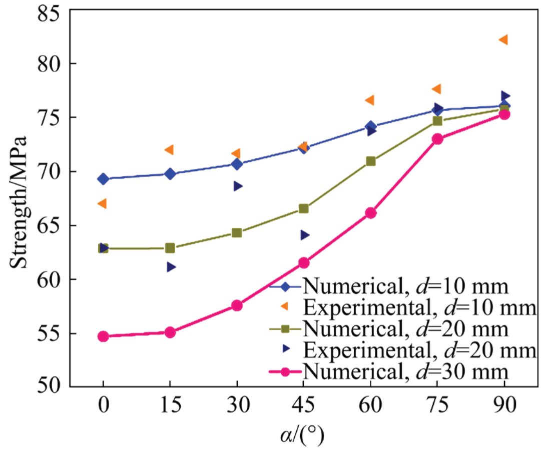

Fig. 7 Numerical and experimental results of dynamic strength of specimens containing surface flaws at different angles and depths

of the simulations are consistent with those obtained from the tests.

On one hand, these results show the accuracy of the simulations, and on the other hand, they show that the strength variation regularities of specimens containing three-dimensional flaws can be obtained by peridynamics using the basic parameters of the rock. In practice, if flaws are encountered parallel to the bearing surface or at an angle less than 60° to the bearing surface, especially when the flaw depth is large, the flaws reduce the strength of the structure significantly. Cracks tend to propagate and cause structural instability, which requires extra attention.

3.2 Crack propagation process

The coordinate axes of the model are shown in Fig. 3, with the center point of the specimen as the origin and the coordinates of the specimen size ranging from −15 mm to 15 mm. In order to study the internal crack propagation process, the simulation results are sliced at different time points using a plane perpendicular to the x-axis. Considering the symmetry of the specimens and loading conditions, all slices are made at x=0, 4, 8, and 12 mm. To avoid repetitive analyses, specimens with a depth of d=10 mm are analyzed at different angles of 0°, 30° and 90°, specimens with a depth of d=20 mm are analyzed at different angles of 0°, 45° and 90°, and specimens with a depth of d=30 mm are analyzed at angles of 0° and 90°.

(1) Flaw depth d=10 mm

Figures 8 and 9 show the failure of specimens containing surface flaws at angles of 0° and 30° at a depth of d=10 mm. As can be seen from the slices for specimen x=0 and 4 mm at 108 μs, the cracks on the surface of the specimen and the shell-like cracks inside the specimen start cracking separately. The crack propagation length on the surface of the specimen is larger than the crack propagation length inside the specimen, indicating that the crack on the surface of the specimen starts earlier and is more likely to propagate than the crack inside the specimen. In addition, wing cracks and anti-wing cracks observed on the surface of the specimen penetrate to a certain depth into the specimen. At

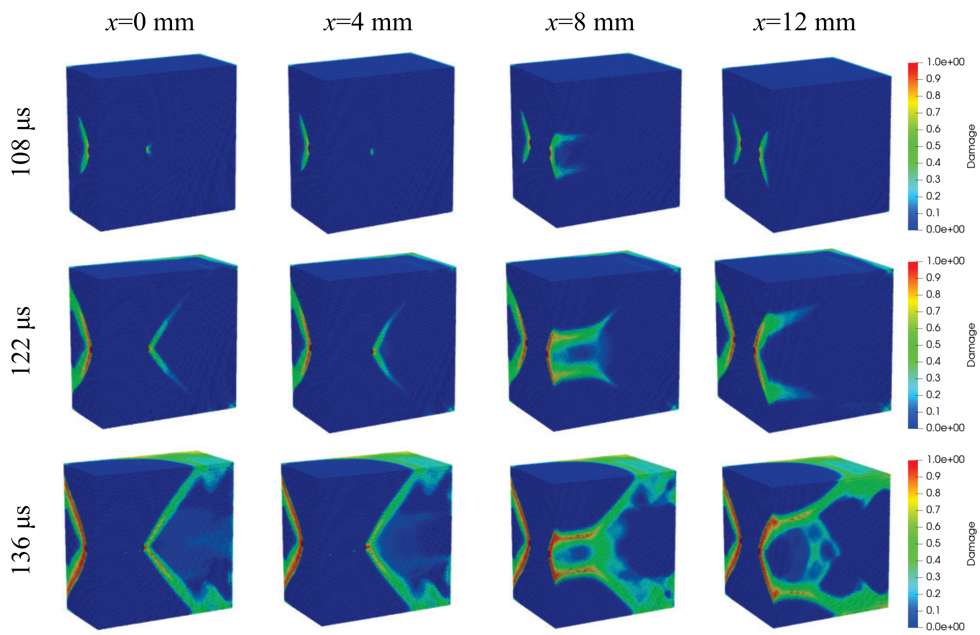

Fig. 8 Failure of specimen with surface flaw depth of d=10 mm and angle of α=0°

122 μs, as can be seen from the slices at x=8 mm, the surface cracks and shell-like cracks connect, with the shell-like cracks propagating along the loading direction towards both the upper and lower parts of the specimen. The shell-like cracks propagate to the end of the specimen at 136 μs. The wing crack of the specimen with a surface flaw angle of 30° joins the shell-like crack first, which is different from the specimen with a surface flaw angle of 0°. From the slices at x=0 mm at 122 μs, it can be seen that the length of shell-like crack propagation decreases with increasing surface flaw angle.

Figure 10 shows the failure of a specimen containing a surface flaw with an angle of 90° and a depth of 10 mm. A small damage zone is formed around the surface flaw at 122 μs. Comparison with Figs. 8 and 9 shows that the crack initiation time is later at a surface flaw angle of 90° than at other angles. At 136 μs, the damage zone expands to the end of the specimen, forming an X-shape damage zone, and the slice at x=0 mm indicates the beginning of shell-like cracks within the specimen. Cracks are formed on the surface of the specimen at 150 μs, and the slice at x=4 mm shows that the cracks on the surface also penetrate to a certain

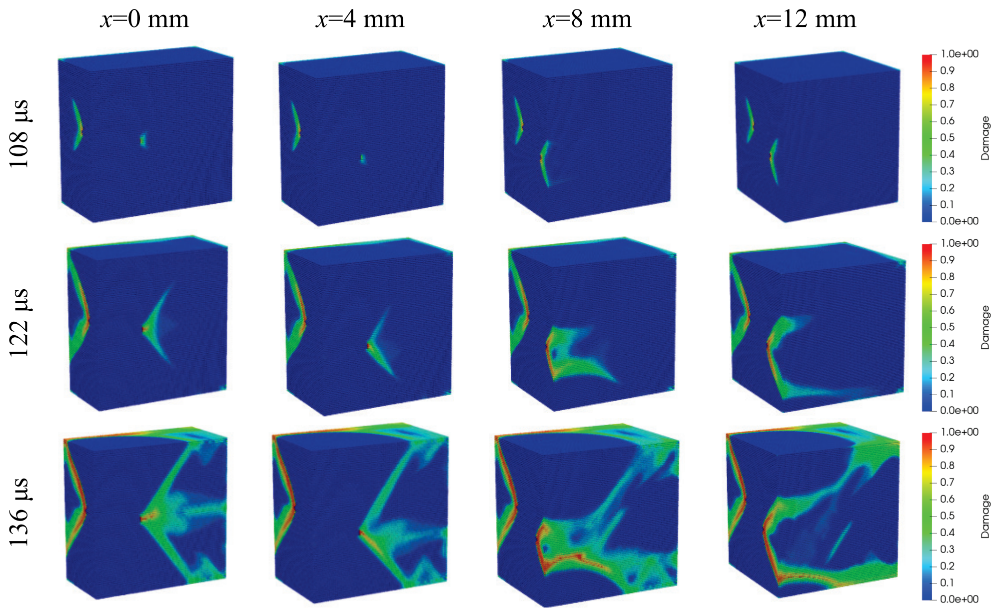

Fig. 9 Failure of specimen with surface flaw depth of d=10 mm and angle of α=30°

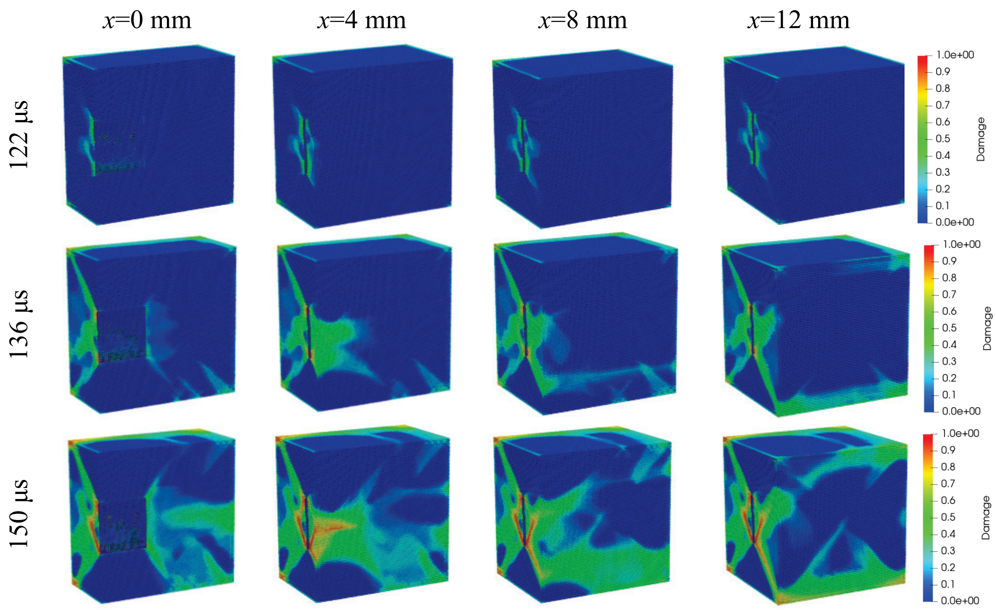

Fig. 10 Failure of specimen with surface flaw depth of d=10 mm and angle of α=90°

depth into the specimen.

(2) Flaw depth d=20 mm

Figures 11 and 12 show the failure of specimens containing surface flaws at angles of 0° and 45° at a depth of d=20 mm. As can be seen from the slices of specimens at x=0 and 4 mm at 108 μs, similar to the specimens containing surface flaws at depth of d=10 mm, the propagation length of the cracks on the surface of the specimens is larger than that of the internal shell-like cracks. The wing and anti-wing cracks generated on the surface of the specimen also penetrate to a certain depth, but at a greater depth for d=20 mm than for d=10 mm. This indicates that the depth of surface wing crack and anti-wing crack initiation on the specimen is related to the depth of the surface flaw, which increases as the surface flaw depth increases. The internal shell-like crack starts at the end of the internal surface flaw in the specimen and is deeper than that in the specimen containing the surface flaw at a depth of d=10 mm. As can be seen from the slice at x=8 mm at 122 μs, the cracks on the surface begin to join with the internal shell-like cracks. Similar to d=10 mm, the wing cracks of the specimen containing the surface flaw at an angle of 45° join the shell-like cracks first, which is different

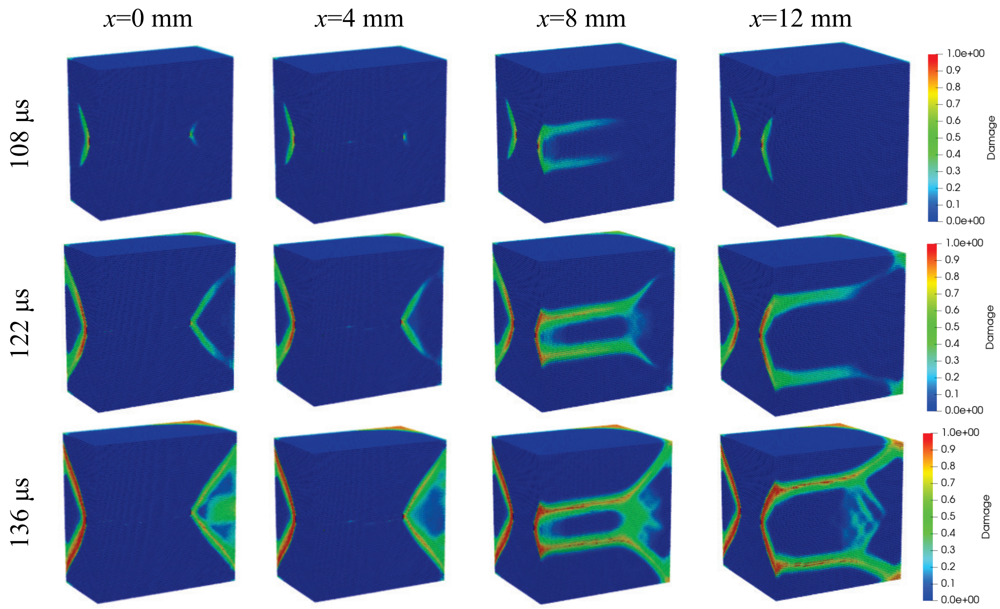

Fig. 11 Failure of specimen with surface flaw depth of d=20 mm and angle of α=0°

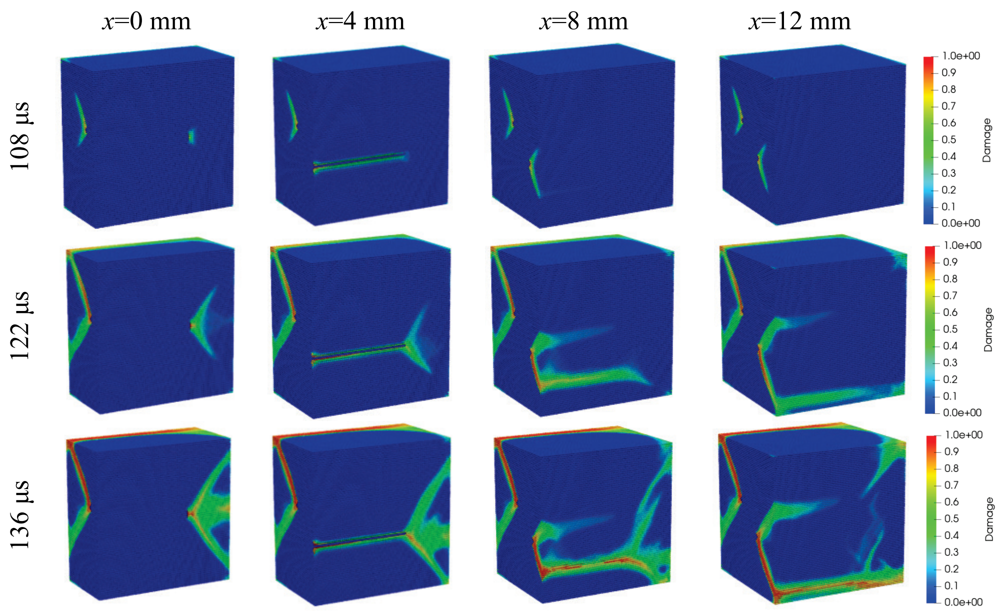

Fig. 12 Failure of specimen with surface flaw depth of d=20 mm and angle of α=45°

from the specimen with a surface flaw angle of 0°.

As can be seen from the slices at x=0 and 4 mm in Fig. 12, the shell-like crack does not initiate at the end of the internal surface flaw of the specimen for the angle of 45° at 108 μs, but only at the middle of the internal surface flaw. At 122 μs, as shown by the slice at x=4 mm, the shell-like crack extends to the end of the internal surface flaw.

Figure 13 shows the failure process of the specimen containing a surface flaw at an angle of 90° and a depth of d=20 mm. At 122 μs, a damage zone appears around the surface flaw. At 136 μs, an X-shaped damage zone similar to that of d=10 mm is formed, and the internal shell-like crack begins to propagate with a slightly larger propagation length than that of d=10 mm. At 150 μs, a crack similar to that at a depth of d=10 mm is formed on the surface of the specimen. The crack on the surface also penetrates to a certain depth inside the specimen, but to a greater depth than in the specimen at depth of d=10 mm.

(3) Flaw depth d=30 mm

Figure 14 shows the failure process of the specimen containing a flaw at an angle of 0° and a depth of d=30 mm. At a flaw angle of 0°, no shell-like crack is formed inside the specimen as the

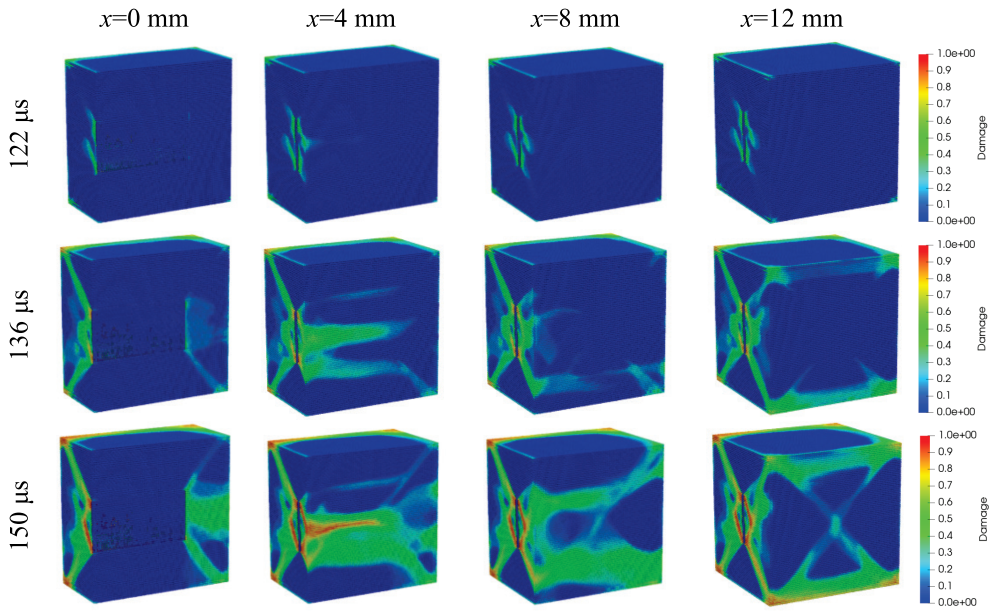

Fig. 13 Failure of specimen with surface flaw depth of d=20 mm and angle of α=90°

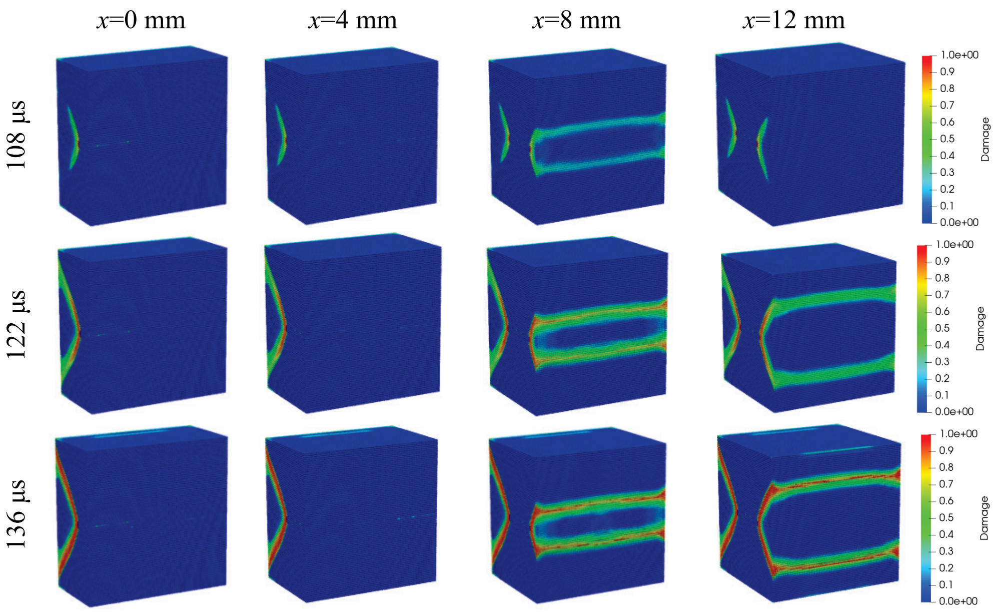

Fig. 14 Failure of specimen with surface flaw depth of d=30 mm and angle of α=0°

crack penetrates it. The crack propagation within the specimen is consistent with the crack propagation on the surface of the specimen, and it can also be regarded as the depth to which the crack propagation generated on the surface penetrates the specimen. The crack propagation is similar to that of the surface-flawed parts of the specimens containing surface flaws to a depth of d=10 and 20 mm.

Figure 15 shows the failure process of the specimen containing a flaw at an angle of 90° and a depth of d=30 mm. At 122 μs, a zone of damage appears around the flaw. At 136 μs, an X-shaped zone of damage is formed through the specimen. At 150 μs, the damage increases further to form a crack through the specimen.

Simulation results for specimens containing surface flaws at angles less than 60° all show wing and anti-wing cracks, which are in good agreement with the test results. The simulated results for specimens containing surface flaws at a depth of d=10 mm and an angle of 75° are similar to the results for specimens at 90°, both of which are somewhat different from those with no tensile cracks appearing in the simulation. The discrepancy between the simulated and experimental results may be due to the non-homogeneity of the rock, and the model used does not take into account the non-homogeneity of the material. It may also be that the defined failure criterion or material model is insufficient to characterize the propagation of tensile cracks in specimens containing three-dimensional flaws under dynamic loading. It is shown that the micro-mechanics of tensile cracking under dynamic loading are more complex and need to be studied in depth.

3.3 Internal cracks and failure modes

The damage values of the material points are filtered, and those with damage greater than 0.85 are taken as cracks. The internal cracks and the final failure mode of the specimen are studied. Figure 16 shows the internal cracks and the final failure pattern of specimens containing surface flaws at angles of 0°, 30°, and 90° at a depth of d=10 mm. At a surface flaw angle of 0°, the shell-like cracks that appear at the end of the surface flaw within the specimen extend to the top and bottom of the specimen. The shell-like cracks join with the surface-generated cracks deep inside the specimen to form a semi-open trumpet-shaped three-dimensional crack. At surface flaw angle of 30°, the wing cracks are the first to extend to the top and bottom of the specimen, and the shell-like cracks extend to the end of the specimen and join with the wing and anti-wing cracks. A shear crack similar to the one on the front surface appears on the back face of the specimen, forming a three-dimensional shear primary crack within the specimen. When the surface flaw angle is 90°, wraparound cracks appear in the vicinity of the surface flaw. A similar X-shaped crack is formed on the surface of the

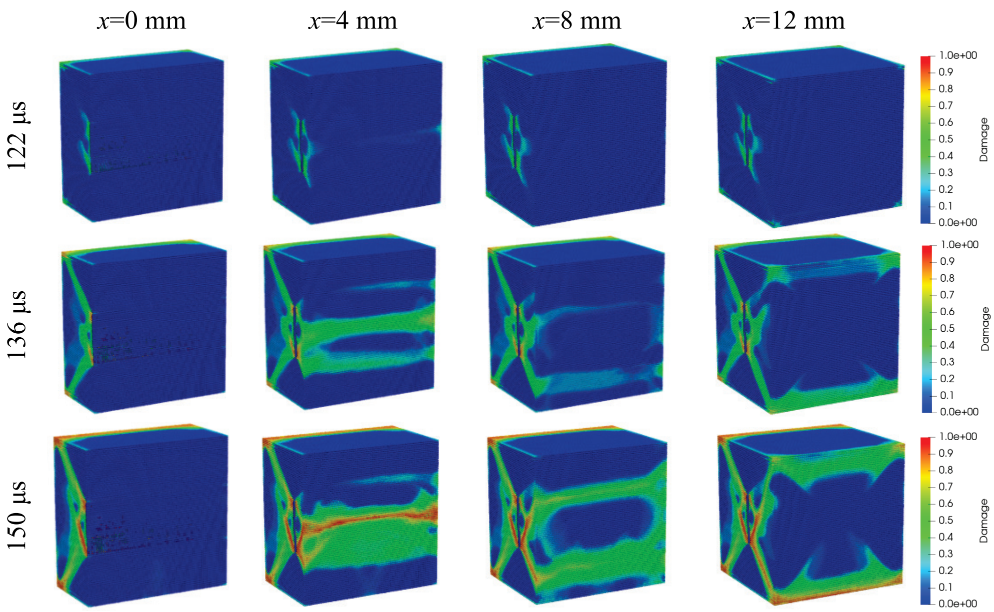

Fig. 15 Failure of specimen with surface flaw depth of d=30 mm and angle of α=90°

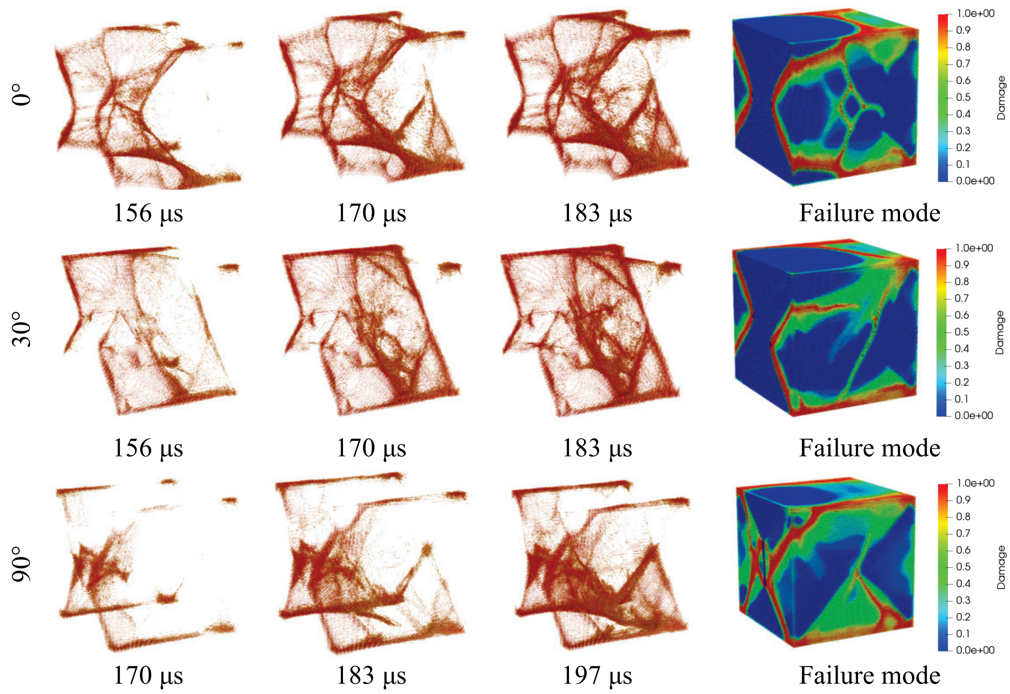

Fig. 16 Internal cracks and failure modes of specimens containing surface flaws at depth of d=10 mm

specimen and penetrates to a certain depth into the specimen, joining the shell-like crack at the bottom inside the specimen.

Figure 17 shows the internal cracks and the final failure pattern of specimens containing surface flaws at angles of 0°, 45°, and 90° at a depth of d=20 mm. As can be seen from the graph, the shell-like cracks within the specimen extend to the top and bottom of the specimen at a surface flaw angle of 0°. The shell-like crack is slightly smaller than that at d=10 mm due to deeper surface flaw, but the depth of the crack formed on the surface of the specimen is larger. The joining of the two produces a three-dimensional crack with a semi-open trumpet shape similar to that of the specimen with a surface flaw at d=10 mm. At a surface flaw angle of 45°, the wing cracks are the first to extend to the top and bottom of the specimen. The shell-like crack joins the wing crack and the anti-wing crack. A shear crack similar to the front surface is formed at the back of the specimen, and a three-dimensional main shear crack is formed within the specimen. At a surface flaw angle of 90°, wraparound cracks appear around the surface flaw. The depth of the wraparound cracks is greater than that of the specimen containing a surface flaw at depth of d=10 mm. The depth of the X-shaped crack is close to the depth of the specimen.

Figure 18 shows the internal cracks and the final failure pattern for specimens with angles of 0° and 90° at depth of d=30 mm. As can be seen from the graph, when the flaw penetrates the specimen and the stress is the same on the specimen scale, the crack propagation on the surface of the specimen is the same as the crack propagation inside the specimen. At a flaw angle of 0°, wing and anti-wing cracks appear at the tips of the flaw and penetrate the entire specimen. At a flaw angle of 90°, wraparound cracks appear around the flaw and penetrate the specimen. An X-shaped crack formed on the surface also penetrates the specimen.

From the above crack propagation process and internal cracks, it can be seen that when the surface flaws do not penetrate the specimen, the shell-like cracks inside the specimen join with the cracks generated on the surface of the specimen to form complex three-dimensional cracks. The cracks formed on the surface penetrate to a certain depth inside the specimen, indicating that the crack propagation on the surface is indicative of the internal crack propagation. The simulation results of this work and those of QIAN et al [14] using RFPA both show the propagation of shell-like cracks inside the specimen. The RFPA results showed shell-like cracks extending towards the front of the specimen, and this simulation shows shell-like cracks extending towards the back of the specimen. The loading waveform in their model

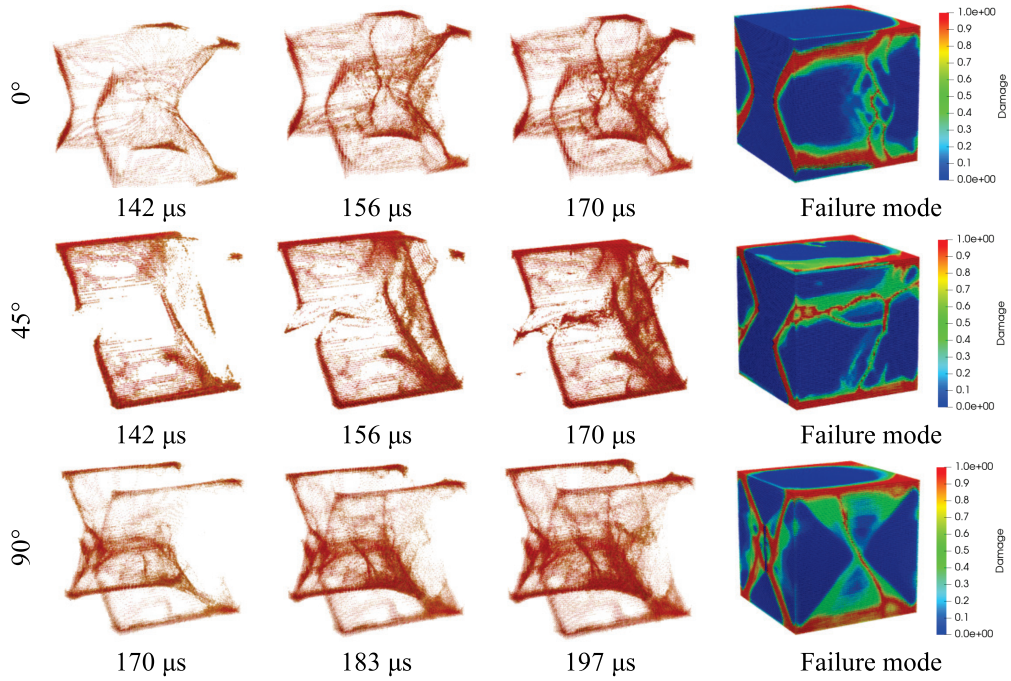

Fig. 17 Internal cracks and failure modes of specimens containing surface flaws at depth of d=20 mm

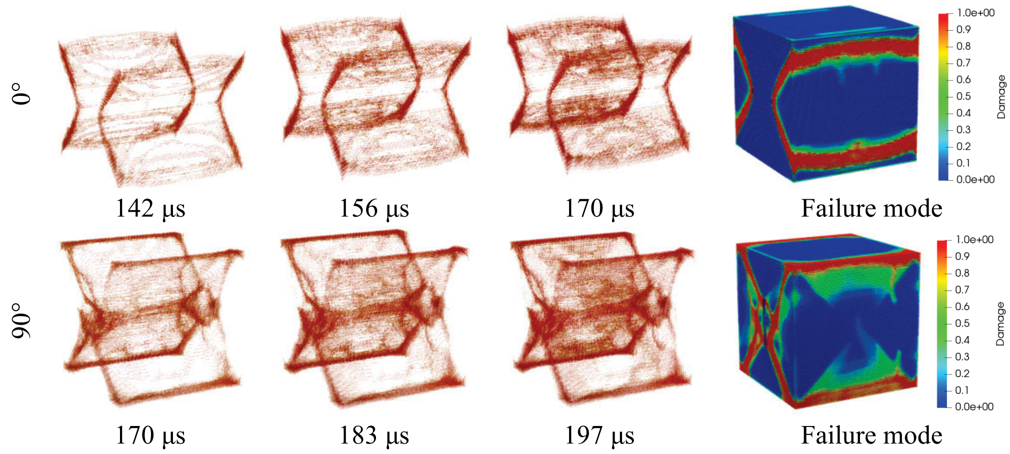

Fig. 18 Internal cracks and failure modes of specimens containing surface flaws at depth of d=30 mm

was a triangular wave, while the loading waveform in this simulation is a half-sine wave. They used rectangular specimens, and this simulation has square specimens. Both the loading waveform and the size of the specimen may affect the three-dimensional crack propagation and need to be investigated further.

4 Conclusions

(1) The elastic−plastic state-based peridynamics that takes into account the ratio of compressive to tensile strengths can simulate three-dimensional rock crack propagation very well. The difference between the compressive and tensile strengths of rocks should be taken into account when modeling damage and fracture with peridynamics.

(2) The dynamic strength of the specimens containing surface flaws increases as the angle of the surface flaws increases. The weakening effect of depth on strength is evident at surface flaw angles less than 60°. When the surface flaw angle is between 75° and 90°, the surface flaw depth has a limited effect on strength. The simulation results are in good agreement with the experimental results, and the peridynamic simulation can be used to obtain a strength variation regularity consistent with the experimental results.

(3) The cracks generated on the surface of the specimen penetrate to a certain depth inside the

specimen, which is related to the depth of the surface flaws. Shell-like cracks extending from the internal surface flaws of the specimen under dynamic loading propagate to the top and bottom of the specimen, connecting with the cracks generated on the surface to form complex three-dimensional cracks.

CRediT authorship contribution statement

Jun ZHANG: Methodology, Visualization, Writing − Original draft, Writing − Review & editing; **Lin-qi HUANG:** Writing − Review & editing; **Zhi-xiang LIU:** Writing − Review & editing; **Xi-bing LI:** Supervision, Writing − Review & editing.

Declaration of competing interest

The authors declare that they have no known competing financial interests or personal relationships that could have appeared to influence the work reported in this paper.

Acknowledgments

This work was supported by the National Natural Science Foundation of China (Nos. 51927808, 51904335, 52174098), and the Fundamental Research Funds for the Central Universities of Central South University, China (No. 2020zzts199).

References

[1] HUANG Lin-qi, WANG Jun, MOMENI A, WANG Shao-feng. Spalling fracture mechanism of granite subjected to dynamic tensile loading [J]. Transactions of Nonferrous Metals Society of China, 2021, 31(7): 2116−2127.

[2] ZHOU Zi-long, LU Jian-you, CAI Xin, RUI Yi-chao. Influence of interface morphology on dynamic behavior and energy dissipation of bi-material discs [J]. Transactions of Nonferrous Metals Society of China, 2022, 32(7): 2339−2352.

[3] WU You, YIN Tu-bing, LIU Xi-ling, TAN Xiao-song, YANG Zheng, LI Qiang. Determination of dynamic mode I fracture toughness of rock at ambient high temperatures using notched semi-circular bend method [J]. Transactions of Nonferrous Metals Society of China, 2022, 32(9): 3036−3050.

[4] LI Xi-bing, FENG Fan, LI Di-yuan. Numerical simulation of rock failure under static and dynamic loading by splitting test of circular ring [J]. Engineering Fracture Mechanics, 2018, 188: 184−201.

[5] LI Xi-bing, ZOU Yang, ZHOU Zi-long. Numerical simulation of the rock SHPB test with a special shape striker based on the discrete element method [J]. Rock Mechanics and Rock Engineering, 2014, 47(5): 1693−1709.

[6] ZHU W C, BAI Y, LI X B, NIU L L. Numerical simulation on rock failure under combined static and dynamic loading during SHPB tests [J]. International Journal of Impact Engineering, 2012, 49: 142−157.

[7] TANG S B. The effect of T-stress on the fracture of brittle rock under compression [J]. International Journal of Rock Mechanics and Mining Sciences, 2015, 79: 86−98.

[8] TANG S B, BAO C Y, LIU H Y. Brittle fracture of rock under combined tensile and compressive loading conditions [J]. Canadian Geotechnical Journal, 2017, 54(1): 88−101.

[9] ZHOU Tao, ZHU Jian-bo, XIE He-ping. Mechanical and volumetric fracturing behaviour of three-dimensional printing rock-like samples under dynamic loading [J]. Rock Mechanics and Rock Engineering, 2020, 53(6): 2855−2864.

[10] ZHOU T, ZHU J B, JU Y, XIE H P. Volumetric fracturing behavior of 3D printed artificial rocks containing single and double 3D internal flaws under static uniaxial compression [J]. Engineering Fracture Mechanics, 2019, 205: 190−204.

[11] PAKZAD R, WANG Shan-yong, SLOAN S W. Three-dimensional finite element simulation of fracture propagation in rock specimens with pre-existing fissure(s) under compression and their strength analysis [J]. International Journal for Numerical and Analytical Methods in Geomechanics, 2020, 44(10): 1472−1494.

[12] MONDAL S, OLSEN K L, GROSS L. Simulating damage evolution and fracture propagation in sandstone containing a preexisting 3-D surface flaw under uniaxial compression [J]. International Journal for Numerical and Analytical Methods in Geomechanics, 2019, 43(7): 1448−1466.

[13] LIANG Z Z, XING H, WANG S Y, WILLIAMS D J, TANG C A. A three-dimensional numerical investigation of the fracture of rock specimens containing a pre-existing surface flaw [J]. Computers and Geotechnics, 2012, 45: 19−33.

[14] QIAN Xi-kun, LIANG Zheng-zhao, LIAO Zhi-yi, WANG Kai. Numerical investigation of dynamic fracture in rock specimens containing a pre-existing surface flaw with different dip angles [J]. Engineering Fracture Mechanics, 2020, 223: 106675.

[15] QIAN Xi-kun, LIANG Zheng-zhao, LIAO Zhi-yi. A three-dimensional numerical investigation of dynamic fracture characteristics of rock specimens with preexisting surface flaws [J]. Advances in Civil Engineering, 2018, 2018: 1−18.

[16] WANG Han, GAO Yong-tao, ZHOU Yu. Experimental and numerical studies of brittle rock-like specimens with unfilled cross fissures under uniaxial compression [J]. Theoretical and Applied Fracture Mechanics, 2022, 117: 103167.

[17] RABCZUK T, BORDAS S, ZI G. A three-dimensional meshfree method for continuous multiple-crack initiation, propagation and junction in statics and dynamics [J]. Computational Mechanics, 2007, 40(3): 473−495.

[18] LIAO Zhi-yi, TANG Chun-an, YANG Wei-min, ZHU Jian-bo. Three-dimensional numerical investigation of rock plate cracking and failure under impact loading [J]. Geomechanics and Geophysics for Geo-Energy and Geo-Resources, 2021, 7(2): 33.

[19] SILLING S A. Reformulation of elasticity theory for discontinuities and long-range forces [J]. Journal of the Mechanics and Physics of Solids, 2000, 48(1): 175−209.

[20] SILLING S A, ASKARI E. A meshfree method based on the peridynamic model of solid mechanics [J]. Computers & Structures, 2005, 83(17/18): 1526−1535.

[21] YU Hai-tao, CHEN Xi-zhuo, SUN Yu-qi. A generalized bond-based peridynamic model for quasi-brittle materials enriched with bond tension–rotation–shear coupling effects [J]. Computer Methods in Applied Mechanics and

Engineering, 2020, 372: 113405.

[22] CHEN Xi-zhuo, YU Hai-tao, ZHU Jian-bo, LIU Jian-feng. A generalized micropolar peridynamic model and its simulation of three-dimensional fracture behaviors [J]. Journal of Tongji University (Natural Science), 2022, 50(4): 463−469. (in Chinese)

[23] AI Di-hao, ZHAO Yue-chao, WANG Qi-fei, LI Cheng-wu. Crack propagation and dynamic properties of coal under SHPB impact loading: Experimental investigation and numerical simulation [J]. Theoretical and Applied Fracture Mechanics, 2020, 105: 102393.

[24] AI Di-hao, ZHAO Yue-chao, WANG Qi-fei, LI Cheng-wu. Experimental and numerical investigation of crack propagation and dynamic properties of rock in SHPB indirect tension test [J]. International Journal of Impact Engineering, 2019, 126: 135−146.

[25] CHEN Zi-guang, NIAZI S, BOBARU F. A peridynamic model for brittle damage and fracture in porous materials [J]. International Journal of Rock Mechanics and Mining Sciences, 2019, 122: 104059.

[26] DIANA V, LABUZ J F, BIOLZI L. Simulating fracture in rock using a micropolar peridynamic formulation [J]. Engineering Fracture Mechanics, 2020, 230: 106985.

[27] ZHOU Zong-qing, LI Zhuo-hui, GAO Cheng-lu, ZHANG Dao-sheng, WANG Mei-xia, WEI Che-che, BAI Song-song. Peridynamic micro-elastoplastic constitutive model and its application in the failure analysis of rock masses [J]. Computers and Geotechnics, 2021, 132: 104037.

[28] FENG Kai, ZHOU Xiao-ping. Peridynamic simulation of the mechanical responses and fracturing behaviors of granite subjected to uniaxial compression based on CT heterogeneous data [J]. Engineering with Computers, 2023, 39: 307−329.

[29] WANG Yun-teng, ZHOU Xiao-ping, KOU Miao-miao. Three-dimensional numerical study on the failure characteristics of intermittent fissures under compressive-shear loads [J]. Acta Geotechnica, 2019, 14(4): 1161−1193.

[30] ZHANG Qing, GU Xin, YU Yang-tian. Peridynamic Simulation for dynamic response of granular materials under impact loading [J]. Chinese Journal of Theoretical and Applied Mechanics, 2016, 48(1): 56−63. (in Chinese)

[31] SILLING S A, EPTON M, WECKNER O, XU J, ASKARI E. Peridynamic states and constitutive modeling [J]. Journal of Elasticity, 2007, 88(2): 151−184.

[32] YANG Sheng-qi, YANG Zhen, ZHANG Peng-chao, TIAN Wen-ling. Experiment and peridynamic simulation on cracking behavior of red sandstone containing a single non-straight fissure under uniaxial compression [J]. Theoretical and Applied Fracture Mechanics, 2020, 108: 102637.

[33] BUTT S N, MESCHKE G. Peridynamic analysis of dynamic fracture: Influence of peridynamic horizon, dimensionality and specimen size [J]. Computational Mechanics, 2021, 67(6): 1719−1745.

[34] ZHOU Xiao-ping, ZHANG Ting, QIAN Qi-hu. A two-dimensional ordinary state-based peridynamic model for plastic deformation based on Drucker−Prager criteria with non-associated flow rule [J]. International Journal of Rock Mechanics and Mining Sciences, 2021, 146: 104857.

[35] ZHOU Xiao-ping, WANG Yun-teng, XU Xiao-min. Numerical simulation of initiation, propagation and coalescence of cracks using the non-ordinary state-based peridynamics [J]. International Journal of Fracture, 2016, 201(2): 213−234.

[36] LI Zheng, GUO De-ping, ZHOU Xiao-ping, WANG Yun-teng. Numerical simulation of crack propagation and coalescence using peridynamics [J]. Rock and Soil Mechanics, 2019, 40(12): 4711−4721. (in Chinese)

[37] CHEN Jing-kai, JIANG Wen-chun, WANG Qi, ZHANG Yan-ting. Peridynamic analysis of drill-induced borehole damage [J]. Engineering Failure Analysis, 2019, 104: 47−66.

[38] ZHANG Jun, HUANG Lin-qi, LI Xi-bing. Experimental study on mechanical properties and failure characteristics of sandstone containing a pre-existing surface flaw under dynamic loading [J]. Engineering Failure Analysis, 2022, 142: 106780.

[39] ERDOGAN M, ERKAN O. Peridynamic theory and its applications [M]. New York: Springer, 2013.

[40] ZOU Chun-jiang, LI Jian-chun, ZHAO Xiao-bao, ZHAO Jian. Why are tensile cracks suppressed under dynamic loading? — Transition strain rate for failure mode [J]. Extreme Mechanics Letters, 2021, 49: 101506.

动载下含表面裂纹岩石破坏的近场动力学模拟

张 俊，黄麟淇，刘志祥，李夕兵

中南大学 资源与安全工程学院，长沙 410083

摘 要：为了研究动态加载下岩石表面裂纹的扩展，基于前期试验结果使用一种考虑压缩和拉伸强度比的弹塑性常规态基近场动力学模型进行数值试验。模拟动态加载下含不同角度和深度三维表面裂纹岩石的破坏过程。模拟结果表明，使用的近场动力学模型可以很好地模拟岩石三维裂纹的扩展和试样的破坏过程。通过近场动力学模拟可以得到与试验结果一致的强度变化规律。试样表面形成的裂纹深入试样内部一定深度，该深度与表面裂纹深度有关。试样内部产生的壳裂纹会与表面形成的裂纹连接形成复杂的三维裂纹。

关键词：动态载荷；表面裂纹；近场动力学；三维裂纹扩展；岩石破坏

(Edited by Bing YANG)